Unique allosteric effect driven rapid adsorption of carbon dioxide in a newly designed ionogel [P_{4444}][2-Op]@MCM-41 with excellent cyclic stability and loading-dependent capacity

Chunfeng Xue[a*], *Hongye Zhu*[a], *Xiao Du*[a], *Xiaowei An*[a], *Enyang Wang*[a], *Donghong Duan*[a], *Lijuan Shi*[a], *Xiaogang Hao*[a*], *Bo Xiao*[b], *Changjun Peng*[c]

[a] *Department of Chemical Engineering, Taiyuan University of Technology, Taiyuan 030024, Shanxi, P. R. China*

[b] *School of Chemistry and Chemical Engineering, Queen's University Belfast, Belfast, BT7-1NN, Northern Ireland, UK.*

[c] *State Key Laboratory of Chemical Engineering and Department of Chemistry, East China University of Science and Technology, Shanghai, 200237, P. R. China*

Abstract: To achieve low cost, high rate and attractive capacity of CO_2 adsorption by using ionic liquid (IL), new mesostructured ionogel, pyridine-containing anion functionalized IL tetrabutylphosphonium 2-hydroxypyridine ([P_{4444}][2-Op]) encapsulated silica MCM-41 (noted as PM-w), is fabricated by loading the IL [P_{4444}][2-Op] with multiple active sites into porous silica MCM-41 through a simple moisture-controlled impregnation-evaporation method. Allosteric effect driven gas sorption on the electronegative oxygen and nitrogen atoms of the nanoconfined IL [P_{4444}][2-Op] makes it take no more than 2 min for the ionogel PM-5 to achieve the 90% of saturated adsorption capacity. Corresponding adsorption rate is 30 times faster than that of the bulk IL. The ionogel PM-5 with the low IL loading of 5% shows the highest CO_2 adsorption capacity up to 1.21 mmol·(g-Ionogel)$^{-1}$ (14.89 mmol·(g-IL)$^{-1}$) at 50 ℃ in a gas mixture with N_2, which is 9.25 times higher than that of the pure IL. Its excellent cyclic stability of more than 96% of the initial CO_2 uptake repeatedly displayed after performing 10 cycles of adsorption-desorption tests. The enhanced thermal stability up to 450 ℃ in N_2 is observed for the low loading ionogels since the strong interfacial layering of the IL preferring to dot the silica nanopores as monomolecular islands. Reversely, the high loading IL may aggregate into nanosized clusters that recover the poor thermal stability of the bulk IL. Reasonable decreasing in their surface area, pore volume and pore size are observed with the IL loading up to 45%. They still exhibit highly ordered hexagonal mesostructure. Featuring with low loading and cost, rapid adsorption, high capacity and excellent cyclic stability make the ionogel PM-5 a competitive candidate in CO_2 capture from the flue gas.

Keywords: Ionic liquid, Ionogel, Mesopore, Allosteric effect, CO_2 capture, Stability, Multiple sites

Formatted: Font color: Auto

1. Introduction

Energy and environmental issues are the main motivation for developing environment friendly materials to capture excessive CO_2 from the combustion of fossil fuel.[1-5] The capture technologies are not only helpful to enhance heat value of natural gas and minimize the global warming but also directly convert CO_2 into final product.[2, 6-7] Current technologies mainly based on organic amines are rather energy intensive and accompanied with serious loss of volatile solvent components.[8-10] New environment concerns are unavoidably triggered by the application processes basing on them. Porous materials including carbon,[3, 11-12] polymer,[13-14] covalent organic framework,[15] and metal organic framework[3, 16-20] were regarded as promising alternatives. Their CO_2 adsorption capacities were also attractive at different evaluation conditions including temperature and pressure. In recent year, viscous ionic liquids (ILs) with basic functional groups have been proposed for developing new CO_2 capture technology due to their negligible volatility, good stability and tunable properties.[10, 21-24] Actually, many attractive CO_2 adsorption capacities have been claimed after the ILs are exposed for very long period to establish the adsorption equilibrium, which mainly results from the ILs' physical properties such as high viscosity, low diffusion coefficients, etc.[10, 25-28]

In order to make full use of the expensive ILs for CO_2 capture, an important strategy is to immobilize or load ILs by incorporation into porous solids to obtain composites called "ionogels".[29-32] Synergistic effect of ionogels are expected to enhance the efficiency of CO_2 adsorption basing on the enlarged interface of gas-liquid.[33] It is reported that the room temperature IL show strong interfacial layering at the support.[34] By experiment and molecular dynamics simulation, it is reported that the interfacial interactions can bring out remarkable changes in the physicochemical properties such as higher viscosity, lower self-diffusion and stronger columbic interactions of nanoconfined ILs than the bulk imidazolium-based IL.[3, 35-36] Porous materials with different structure are used to load different ILs and show various gas adsorption performances. Intercalated materials are co-assembled from imidazolium-based IL and layered nanosheet show adsorption capacity of 0.73 $mmol \cdot g^{-1}$ due to the exposure of the functional groups of the IL.[37] The IL tetrabutylphosphonium amino acid supported on silica gel show 50% adsorption capacity of the pure IL.[38] Their adsorption rates are as slow as the pure ILs. Similar result was observed in the studied of mesoporous silica MCM-41 loaded with IL $[P_{66614}][2\text{-Op}]$.[39] In 2014, two ILs immobilized on porous alumina and silica respectively show the similar thermal stability to those of the pure ones and equimolar

Formatted: Font color: Auto
Formatted: Font color: Auto
Formatted: Font color: Auto
Formatted: Font color: Auto
Formatted: Font color: Auto
Formatted: Font color: Auto
Formatted: Font color: Auto
Formatted: Font color: Auto
Formatted: Font color: Auto
Formatted: Font color: Auto
Formatted: Font color: Auto
Formatted: Font color: Auto
Formatted: Font color: Auto
Formatted: Font color: Auto
Formatted: Font color: Auto
Formatted: Font color: Auto
Formatted: Font color: Auto
Formatted: Font color: Auto
Formatted: Font color: Auto
Formatted: Font color: Auto
Formatted: Font color: Auto
Formatted: Font color: Auto
Formatted: Font color: Auto
Formatted: Font color: Auto
Formatted: Font color: Auto
Formatted: Font color: Auto
Formatted: Font color: Auto
Formatted: Font color: Auto
Formatted: Font color: Auto
Formatted: Font color: Auto
Formatted: Font color: Auto

CO_2 capture at 120 °C.[40] The imidazolium-based IL is also immobilized in functional group grafted mesoporous silica show adsorption capacity up to 11 w/wt% at 2.0 MPa.[41] Nanoporous polymethylmethacrylate microspheres impregnated with amino acid ILs show CO_2 adsorption capacity 1.3 – 1.53 mmol·g^{-1} at 40 °C.[42-43] High adsorption capacities are also observed on mesoporous silica supported hydroxyalkyl amidines.[44] The various silica surface-confined zinc-functionalized ILs take 20,000 second to achieve adsorption capacity up to 2 – 4.7 mmol·g^{-1} at 40 °C.[45-47] Obviously, most of the above ionogels show good adsorption capacities but poor cyclic stability as well as low adsorption rate, which may impede their potential applications. At all events, it is urgent that a reasonable ionogel for rapid adsorption, high capacity and good cyclic stability should be designed by loading a well-chosen IL into a porous supporter with high surface area.

After considering the multiple-site cooperative interactions of pyridine-containing anion and the small free volume of tetrabutylphosphonium cation $[P_{4444}]^+$, we carefully fabricated ionogels, IL tetrabutylphosphonium 2-hydroxypyridine ($[P_{4444}][2\text{-Op}]$) encapsulated into silica MCM-41 (denoted as PM-ws), for CO_2 capture by lining the designed IL ($[P_{4444}][2\text{-Op}]$) composed of $[P_{4444}]^+$ and $[2\text{-Op}]^-$ into mesoporous supporter MCM-41. The ionogel PM-ws exhibit highly ordered hexagonal mesostructure. With only 5 % IL $[P_{4444}][2\text{-Op}]$ lining in the ionogel PM-5, the highest CO_2 adsorption capacity is observed up to 1.21 mmol·(g-Ionogel)$^{-1}$ (14.89 mmol·(g-IL)$^{-1}$) at 50 °C in a CO_2/N_2 mixture, which is much higher than that of the pristine IL. Allosteric effect driven stepwise gas sorption on the electronegative oxygen and nitrogen atoms of the IL makes its 90% of saturated adsorption capacity achieve in no more than 2 min, which is fairly faster than the bulk IL and other reported materials. Almost 97 % of the initial CO_2 uptake is maintained after performing 10 cycles of adsorption-desorption tests. Also, an enhanced thermal stability up to 450 °C in N_2 is observed for the low loading ionogels.

2. Experiment section

2.1 Chemicals

Tetrabutylphosphonium hydroxide solution ($[P_{4444}][OH]$, 40 % in H_2O) and 2-hydroxypyridine (2-Op, > 98 %) were purchased on J&K Scientific Ltd. Mesoporous silica MCM-41 from Catalyst Factory of Nankai University was calcined at 500 °C for 4 h before use. Anhydrous ethanol was purchased fro Tianjin Zhiyuan Chemical Reagent Co., Ltd. N_2 (> 99.99 %), CO_2 (> 99.99 %) was bought from Taiyuan Taineng Gas Co. Ltd.

Formatted: Font color: Auto
Formatted: Font color: Auto
Formatted: Font color: Auto
Formatted: Font color: Auto
Formatted: Font color: Auto
Formatted: Font color: Auto
Formatted: Font color: Auto
Formatted: Font color: Auto
Formatted: Font color: Auto
Formatted: Font color: Auto

2.2 Preparation of pyridine-containing anion functionalized IL [P_{4444}][2-Op]

The IL [P_{4444}][2-Op] was prepared according to the reported method,[48] wherein some modification in the process. 9.77~~44~~ g [P_{4444}][OH] was dissolved in 20 mL ethanol and stirred at room temperature. Then, 1.34~~50~~ g 2-Op was dissolved in another 20 mL ethanol. Subsequently, the two solutions were mixed at 30 ℃ for 24 h and evaporated in rotary evaporator at 50 ℃ for 1 h. After further drying it at 60 °C under vacuum for 48 h, we obtained the IL finally. Compared with the viscosity of water (0.55 mPa·s), the IL viscosity was measured to be 202 mPa·s with an accuracy of 3.33 mPa·s, showing fairly high viscosity. Its molecular weight is calculated at 353.53. Its density determined at 0.85~~07~~ g·cm^{-3} by using a pycnometer and calibrated by water. CO_2 adsorption capacity of the pure IL is measured at 1.61 mmol·g^{-1} by bubbling CO_2 at 50 ℃ for 100 min (**Fig. S1**). Besides, ^{13}C NMR (500 MHz, DMSO, 25 ℃) of IL [P_{4444}][2-Op]: δ = 13.3, 14.1, 18.6, 18.9, 23.6, 23.7, 23.8, 23.9, 24.3, 27.3, 27.8, 105.5, 120.1, 132.2, 139.7, 160.4 ppm (**Fig. S2**); ^{31}P NMR (500 MHz, DMSO, 25 ℃) of the IL: δ = 33.8 ppm.

2.3 Preparation of ionogels by lining IL [P_{4444}][2-Op] into mesostructured MCM-41

The ionogel sample was prepared basically according to the impregnation-evaporation method.[49] In view to the poor hydrothermal stability of MCM-41, the water content of the IL in our experiments is strictly controlled less than 0.54 %. A given amount of the dried IL was dissolved in 30.0 g of ethanol and stirred for 1 h at room temperature. Then, 1.0 g of the calcined MCM-41 was added into the solution and mixed at 80 ℃ for 2 h. The resultant mixture was evaporated at 80 ℃ for 3 h and dried in vacuum oven at 100 ℃ for further 12 h to remove deionized water and ethanol. According to the loading amount of IL [P_{4444}][2-Op], obtained iongels [P_{4444}][2-Op]@MCM-41 are denoted as PM-w, where "w" means weight percentage of IL [P_{4444}][2-Op] in the initial reaction mixture. Briefly, we prepared ionogels PM-1, PM-3, PM-5, PM-10, PM-15, PM-30, and PM-45 for further investigation respectively.

2.4 Characterization

Powder X-ray diffraction (PXRD) of samples were collected on Rigaku Ultima IV type X-ray diffractometer, equipped with the Cu Kα radiation, (λ= 0.154056 nm, 40 kV, 40 mA) with a scan range of 1 – 7°. N_2 adsorption-desorption isotherms were measured on JW-BK122W specific surface area and pore size analyzer at –196 ℃. Mesoporous silica MCM-41 (100 – 200 mg) was degassed at 300 ℃ for 3 h under vacuum before measurement, while ionogels PM-ws (100 – 200 mg) were degassed at 120 ℃ for 8 h. Specific surface area of samples were estimated by using Brunauer-Emmett-Teller (BET) method. The

pore size distributions were calculated with Barrett-Joyner-Halenda (BJH) method on the basis of adsorption branches of the isotherms. Fourier transfer infrared spectroscopy (FT-IR) spectrum of all the samples were recorded with a solution of 2 cm^{-1} in the range of 400 – 4000 cm^{-1} on a Thero Nicolet-360 FT-IR spectrometer using KBr as the window material. ^{31}P NMR and ^{13}C NMR spectra of 0.5 mL of IL [P_{4444}][2-Op] were recorded on Bruker DRX 500 MHz. The viscosity was measured on Brookfield DV2T viscometer with a 53 mm spindle. Scanning electronic micrographs of samples were collected on a JSM-6700F field-emission scanning electronic microscopy, all the samples were sputter-coated with gold be fore the testing. The water content of sample was measured on AKF-3 Karl Fischer coulometer. Thermogravimetry (TG) curves of samples were collected on a Netzsch STA 449 F5 TG/DTG instrument. About 7.0 mg of samples were placed onto an alumina crucible and heated at a ramp of 10 °C·min^{-1} in the range of from 30 to 800 °C in N_2 flow (100 mL·min^{-1}) to analyze thermal stability of ionogels.

2.5 Studies on CO_2 adsorption capacity

CO_2 adsorption capacity of ionogels PM-ws were calculated by recording breakthrough curves on Gasboard-3100 gas analyzer as shown in **Fig. S3**. 1.0 g of dried ionogel PM-w was placed into the sample tube with an inner diameter of 10.0 mm and a length of 220.0 mm, the height of samples about 100.0 mm. First, the sample was treated at 120 ℃ for 2 h in N_2 flow of 98.5 mL·min^{-1} before testing to remove trace water and adsorbed gas impurities. Then it was cooled to given adsorption temperature (50 ℃), which referred to typical temperature range of flue gas. Next, a mixed CO_2/N_2 gas was introduced into CO_2 analyzer via bypass until the concentration of CO_2 was constant, in which the volume concentration of CO_2 was approximate 14.5 vol.% in N_2 balance at a flow rate of 98.5 mL·min^{-1}. The CO_2 gas and N_2 gas was controlled by mass flow controller DO7-11C (Beijing) separately. Afterwards, the mixed CO_2/N_2 gas was switched to the sample tube at 50 ℃ to perform the adsorption experiment. The reaction was continued until the adsorption saturation was achieved. In other words, the experiment was completed when CO_2 analyzer shows a constant CO_2 concentration was equal to start value. The CO_2 adsorption capacity (q, mmol·(g-Ionogel)$^{-1}$) of calcined supporter MCM-41 and ionogel PM-ws at a certain time (t, s) was calculated from the equation as below,

$$q = \int_0^t Q(c_{in} - c_{eff})dt \Big/ (mv_m)$$

Formatted: Font color: Auto

Formatted: Font color: Auto

Where m represents the weight of the iongel (g). Q is the influent flow rate (mL·min^{-1}). C_{in} and C_{eff} are the influent and effluent CO_2 concentration (vol.%), respectively. The v_m is standard molar volume (22.4

mL·mmol^{-1}). Herein, ionogel PM-5 was chosen to investigate the cyclic stability in 10 cycles of adsorption and regeneration test. The process of regeneration was conducted in the pure N_2 flow of 98.5 mL·min^{-1} at 120 ℃ for 1 h

3. Results and discussion

3.1 Stepwise CO_2 *adsorption on the nanoconfined IL with multiple active sites*

The structure of pyridine-containing anion functionalized IL [P_{4444}][2-Op] is confirmed by comparing its FTIR pattern with the raw materials. The bands at around 2936 cm^{-1} ascribed to stretching vibration of –CH_3 group is observed for raw material [P_{4444}][OH] and IL [P_{4444}][2-Op] (**Fig. 1 A (a)** and **(c)**).[50] The bands at 1640, 1600 and 1535 cm^{-1} of N–H bending vibration are observed in the spectra of both 2-Op and IL [P_{4444}][2-Op] (**Fig. 1 A (b)** and **(c)**), indicating the successful combination of [P_{4444}][OH] and 2-Op. Additionally, the spectra of the ionogels PM-5, PM-45 and calcined supporter MCM-41 show that an internal asymmetric stretching vibration from Si-O band at 1105 cm^{-1} (**Fig. 1 A (d)-(, e, and f)**). Just as expected, some bands at around 2936 cm^{-1} also present in the spectra of ionogels PM-5 and PM-45 (**Fig. 1 A (c)** –, **d and (e)**). Reasonably, their intensities of high loading ionogel PM-45 are stronger than those of low loading ionogel PM-5 but weaker than the bulk IL.

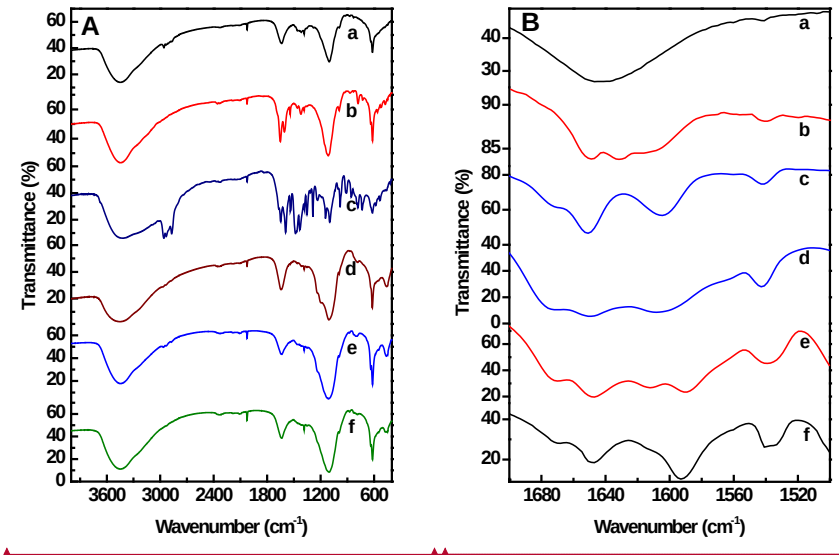

Fig. 1 FTIR spectra (A) of samples: (a) raw material [P_{4444}][OH], (b) raw material 2-Op, (c) IL

Formatted: Font color: Auto
Formatted: Font color: Auto
Formatted: Font color: Auto
Formatted: Font color: Auto
Formatted: Font color: Auto
Formatted: Font color: Auto

[P_{4444}][2-Op], (d) PM-5, (e) PM-45 and (f) calcined MCM-41; FTIR spectra range from 1500 to 1700 cm^{-1} (B) of samples: (a) ionogel PM-5, (b) ionogel PM-5 with CO_2 adsorption interrupted at 20 seconds, (c) ionogel PM-5 with saturated CO_2 adsorption after exposure in CO_2/N_2 for 285 seconds, (d) the IL with saturated CO_2 adsorption after exposure in CO_2 for 7200 seconds, (e) the IL with CO_2 adsorption interrupted at 1200 seconds, and (f) fresh bulk IL [P_{4444}][2-Op]

For the IL with multiple active sites, it is important to find the CO_2 adsorption order of the oxygen and nitrogen atoms. FT-IR patterns in the range of 1500 – 1700 cm^{-1} of ionogel PM-5 and bulk IL with partial or saturated CO_2 adsorption are selected for careful investigation (**Fig. 1 B**). Ionogel PM-5 shows a broad band at about 1643 cm^{-1}, assigned to stretching vibration of bonds C=O and C=C (**Fig. 1 B (a)**). After it is exposed in CO_2/N_2 for 20 seconds, it shows a new band at 1630 cm^{-1} accompanied with a shoulder band at around 1610 cm^{-1} (**Fig. 1 B (b)**), which can be indexed as the coordinate bonds C←O and C←N respectively. Their different strengths imply CO_2 predominantly binds with oxygen atoms due to its calculated large Mulliken electro-negativity (–0.643) and the promotion from the allosteric effect of nitrogen atoms binding with scarce CO_2 molecule in the initial adsorption. Similar results is also observed in the studies on the bulk IL [P_{66614}][2-Op].[28] In case of ionogel PM-5 with saturated CO_2 adsorption, the strong band at 1605 cm^{-1} indicates the blue shift and the mergence of the bands 1610 and 1630 cm^{-1} (**Fig. 1 B (c)**). This is because their changed steric configuration and the increasing bonds C←N in that more and more CO_2 molecules coordinating with nitrogen atoms during the second half adsorption. Similar features can be found in CO_2 saturated adsorption of bulk IL (**Fig. 1 B(d)**). The IL with partial CO_2 adsorption show a strong band at 1610 cm^{-1} and the nearly disappearing one at 1625 cm^{-1}, indexed as the coordinate bonds C←N and C←O respectively (**Fig. 1 B (e)**). By comparing with the fresh IL (**Fig. 1 B (f)**), we find that a red shift occurred on the band at 1593 cm^{-1} corresponding to the bond C–O stretching vibration during the CO_2 adsorption. Therefore during the second half adsorption, the CO_2 molecules are predominantly binding with nitrogen atoms whose activity is triggered by allosteric effect mainly from the oxygen atoms of the IL saturated with CO_2. Thus, it is easily understandable that the band at 1610 cm^{-1} ascribed to bonds C←N turns strong enough to swallow the one at 1625 cm^{-1} ascribed to the coordinate bonds C←O. In summary, the nitrogen and oxygen atoms successively acts as allosteric sites to its counterpart during the rapidly stepwise CO_2 adsorption process.

3.2 Status-dependent thermal stability of the nanoconfined IL

Formatted: Font color: Auto

Formatted: Font color: Auto

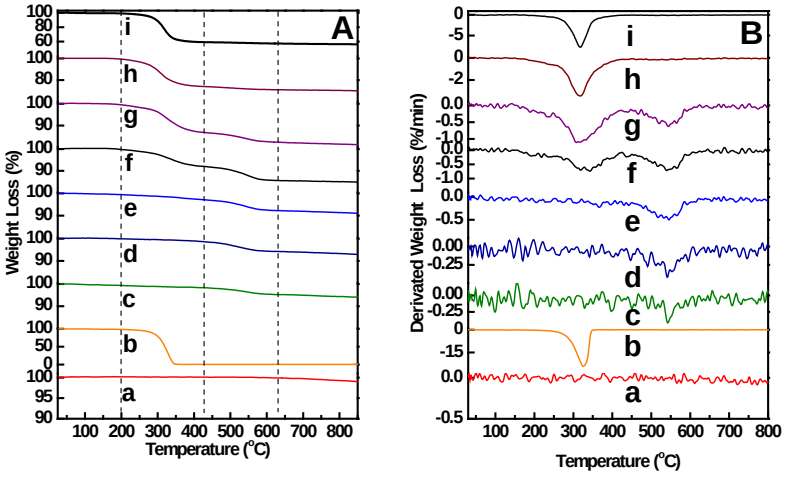

Fig. 2 (A) TG and (B) DTG curves of the samples: (a) Calcined MCM-41; (b) Bulk IL; (c) PM-1, (d) PM-3, (e) PM-5, (f) PM-10, (g) PM-15, (h) PM-30, and (i) PM-45.

Dramatically enhanced thermal stability of ionogel PM-ws mainly benefit to the excellent cyclic stability. Their thermal stability are observed from their TG curves by comparing with the bulk IL $[P_{4444}][2\text{-Op}]$. As can be seen in **Fig. 2**, the calcined supporter MCM-41 shows a total weight loss of 1.1%, which due to the removal of partial hydroxyl at high temperature above 550 °C (**Fig. 2A (a)**). Only a slight weight loss of 0.38% is observed for the pure IL $[P_{4444}][2\text{-Op}]$ below 100 °C, basically ascribed to its physical water content of 0.54% measured on AKF-3 Karl Fischer coulometer. An obvious weight loss up to 99% is further observed for it in range from 100 to 320 °C, which can be ascribed to its initial evaporation and subsequent bulk decomposition (**Fig. 2A (b)**). Accordingly, it approximately starts to decompose at 200 °C. While the IL immobilized in different ionogels exhibit dis behaviors. As can be seen in **Fig. 2A (c), d, and (e)**, it is reasonable that total weight losses of ionogels PM-1, PM-3 and PM-5 gradually enhance with increasingly loaded IL $[P_{4444}][2\text{-Op}]$. Noticeably, their weight losses mainly occur above 450 °C, which obviously higher than the onset decompositio temperature of the bulk IL. The results indicate that their thermal stability are enhanced by more than 250 °C, which is the highest magnitude of enhancement on therm in conducting matrices as far as we known.[50-52] The results are different from the decreased stability of

Formatted: Font color: Auto

Formatted: Font color: Auto

Formatted: Font color: Auto

other IL on the similar non-conducting matrices of silica.[50] They can be attributed to significant interfacial layering and stiffening of the immobilized IL in the vicinity of the supporter surface as well as the lower self-diffusivity at low IL loading caused by the nanospace confinement effect.[35] The results imply that low content IL mainly dots the mesopore surface of the supporter MCM-41 forming surface flecks, in which the substrate wall-IL interaction slows down the dynamics.[50] The excellent thermal stability allows the maximum operation temperature up to 450 ℃ without any mass loss and may endow remarkable cyclic stability. With further infusion of the IL [P_{4444}][2-Op] up to 15%, two obvious weight losses are observed for ionogels PM-10 and PM-15 (**Fig. 2** ~~**A**~~ (**f**) and (**g**) ~~and **Fig. 2 B (f and g)**~~) in the ranges of 200 – 420 ℃ and 430 – 630 ℃, respectively. The former may correspond to the decomposition of aggregating IL in mesopores and the latter to that of nanospace confined one respectively. The results imply that the IL locates in at least two different circumstances or statuses. It is reasonable that the weight loss of PM-10 at the low temperature range is no more than that of PM-15 because of its relatively low loading. Noticeably, the ionogel PM-10 displays about a weight loss of 6.49 % at the high temperature range, which is obviously larger than 4.47 % of PM-15. The results reveal that the IL prefers to form surface flecks in the mesopores and then turn into oligomers or nanosized clusters which show low onset decomposition temperature due to the thronging IL. The properties of the IL molecules inside the oligomers or nanosized clusters are mainly controlled by the fluid-fluid interaction and insignificant effect of the substrate-fluid interaction.[50] As a result, the viscosity as well as the thermal stability in this layer is low as the bulk IL. Similar research results on the imidazolium-based ionogels even show poorer thermal stability than the free IL.[53] Interestingly, with further loading of the IL [P_{4444}][2-Op] up to 45 %, weight losses are mainly observed for PM-30 and PM-45 in the exclusive range of 200 – 420 ℃, which is close to that for free IL. No obvious weight loss temperature assigned to the enhancement on thermal stability is observed for them. The results imply that all the IL is immobilized in a similar aggregation status such nanosized clusters, in which the strong interfacial layering exponentially decay into the bulk IL (**Fig. 2-A** (**h**) and (**i**)).[34] The results also well agree with their lowering hysteresis loops of N_2 sorption isotherms below and other reported high loading ionogels.[37, 40] Combining the evolution rhythm of onset decomposition with the IL loading, we believe that there is a threshold value responsible for loading-dependent status on the supporter just as the value in the nanotube diameter for the IL $ChZnCl_3$ filling.[52] Supposedly, the threshold lining value for a highly thermally stable ionogel is about 5%. Although the absence of images on the loading-dependent

Formatted: Font color: Auto
Formatted: Font color: Auto
Formatted: Font color: Auto
Formatted: Font color: Auto
Formatted: Font color: Auto
Formatted: Font color: Auto
Formatted: Font color: Auto
Formatted: Font color: Auto
Formatted: Font color: Auto
Formatted: Font color: Auto
Formatted: Font color: Auto
Formatted: Font color: Auto
Formatted: Font color: Auto
Formatted: Font color: Auto
Formatted: Font color: Auto
Formatted: Font color: Auto

morphology of the immobilized IL as the size-dependent morphology of IL $ChZnCl_3$ in the carbon nanotube,[52] the IL in a monomolecule island-like pattern dots the mesoporous silica inside basing on the surface property and pore size of the calcined supporter MCM-41 as well as the IL. The threshold loading value for the presence of two kinds of dispersing status should be between 5% and 15%. Part of the IL aggregates into oligomers as a result of recovering the property of the bulk IL. Probably, more than 15% is the threshold impregnating value for the loading-dependent status of all the immobilized IL gathering as nanoclusters, which show the same properties to the bulk IL.

3.3 Loading-dependent mesostructure of the ionogel

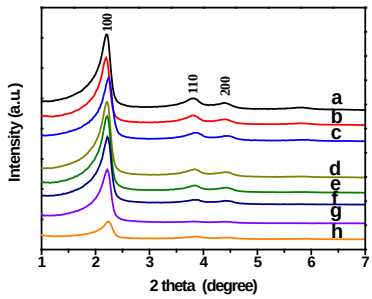

Fig. 3 Low angle XRD patterns of samples: (a) calcined MCM-41~~,~~; (b) PM-1, (c) PM-3, (d) PM-5, (e) PM-10, (f) PM-15, (g) PM-30, and (h) PM-45.

Low angle XRD patterns of calcined porous silica MCM-41 and ionogel PM-ws reveal their highly ordered mesostructure (**Fig. 3**). In details, the calcined supporter MCM-41 shows three well-resolved peaks and weak one (**Fig. 3 (a)**), indicating a highly ordered mesostructure. The three characteristic reflections at 2θ = 2.2°, 3.8° and 4.4° can be indexed as the planes of (100), (110) and (200) respectively, implying a hexagonally mesoporous structure.[54-57] When the IL $[P_{4444}][2\text{-Op}]$ up to 10 % is loaded into the supporter, no obvious change in the intensity of three peaks is observed for the corresponding ionogels PM-1, PM-3, PM-5, and PM-10 except the decaying weak peak at around 2θ = 5.83° (**Fig. 3 (b) ~~, c, d, and~~ (e)**). The results indicate that the ordered mesostructure of supporter MCM-41 is perfectly maintained using the modified preparation process, in which the water content of IL is strictly controlled below 1.0 % due to the poor hydrothermal stability of MCM-41. At the same time, the slightly decaying reflections nicely imply the mesopores are successfully lined with the IL $[P_{4444}][2\text{-Op}]$. When the

Formatted: Font color: Auto
Formatted: Font color: Auto
Formatted: Font color: Auto
Formatted: Font color: Auto
Formatted: Font color: Auto
Formatted: Font color: Auto

impregnated amounts of IL [P_{4444}][2-Op] are beyond 10.0 %, the intensities of all three well-resolved peaks are obviously lowering in ionogels PM-15, PM-30, and PM-45 (**Fig. 3 (f, g,** and **h)**), which is ascribed to the IL further filling into the mesopores. Such changes on the intensity of reflections caused by guest species in channels are common for porous materials and do not really reflect the reduction of ordered mesostructure. For example, XRD peaks' intensities of calcined MCM-41 are always stronger than those of template-containing as-made MCM-41.[54] Thus, whatever the IL loading is as low as 1.0 % or high as 45.0 %, highly ordered mesoporous ionogels are prepared by using the moisture-controlled impregnation-evaporation method.

3.4 Morphology of the ionogels

Morphology images of all the samples are collected on field-emission scanning electronic microscopy (FESEM). The calcined supporter MCM-41 shows irregular particles aggregated from tiny amorphous species with diameters of around 1.0 micrometer (**Fig. 4 (a** and **b)**). All the iongels with different loading of IL exhibit similar irregular shapes to the supporter (**Fig. 4 (c**, **d**, **e**, **f**, **g**, **h** and **i)**). No obvious IL can be found on the external surface of the particles. The results imply that the structures of iongels are very stable during the preparation and independent of the loading amounts from 1.0 % to 45.0 %.

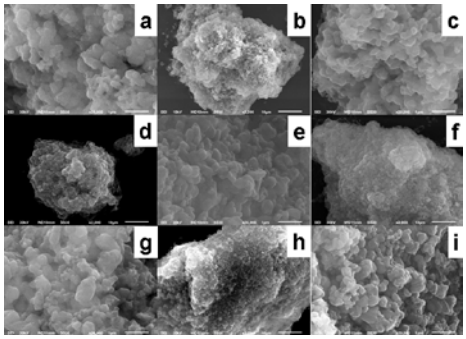

Fig. 4 FESEM images of samples: (a) (, b) calcined MCM-41; (c) PM-1, (d) PM-3, (e) PM-5, (f) PM-10, (g) PM-15, (h) PM-30, and (i) PM-45.

3.5 Loading-dependent porosity of the ionogels

Formatted: Font color: Auto

Formatted: Font color: Auto

Formatted: Font color: Auto

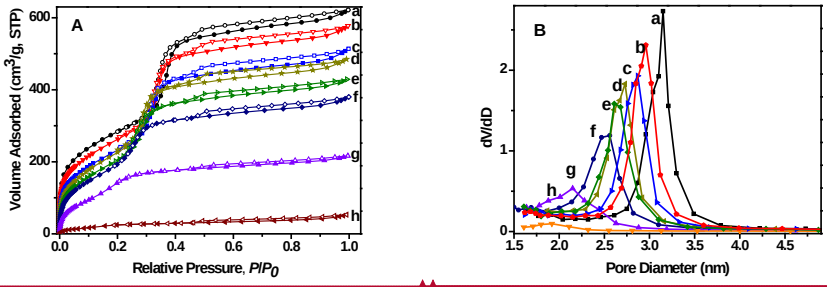

Fig. 5 N_2 adsorption isotherms (A) and pore size distributions (B) of samples: (a) calcined MCM-41, (b) PM-1, (c) PM-3, (d) PM-5, (e) PM-10, (f) PM-15, (g) PM-30, and (h) PM-45.

Table 1. Textural characteristics of the supporter MCM-41 and ionogels PM-ws

Sample	Surface area ($m^2 \cdot g^{-1}$)	Pore diameter (nm)	Pore volume ($cm^3 \cdot g^{-1}$)
MCM-41	1038.1	3.15	0.96
PM-1	939.3	2.96	0.89
PM-3	851.4	2.87	0.79
PM-5	830.8	2.73	0.75
PM-10	759.8	2.61	0.66
PM-15	697.4	2.56	0.59
PM-30	422.5	2.14	0.33
PM-45	86.7	1.92	0.08

N_2 adsorption-desorption isotherms and corresponding pore size distributions of ionogel PM-ws are summarized in **Fig. 5**. The calcined MCM-41 shows a type IV isotherm with two obvious hysteresis loops at relative pressures P/P_0 = 0.25 – 0.40 and 0.40 – 0.95 (**Fig. 5 A (a)**), indicating the presence of uniform mesopores and particle-stacked macropores.[57] Its BET surface area is calculated about 1038.1 $m^2 \cdot g^{-1}$. Its pore size distribution is narrow and centers at 3.15 nm (**Fig. 5 B (a)**). No obvious macropore distribution is observed for them, implying that the amount of macropores is rather limited. Its total pore volume is as high as 0.96 $cm^3 \cdot g^{-1}$ (**Table 1**). After increasingly impregnated with IL [P_{4444}][2-Op] up to 30%, although all the isotherms of the ionogels still keep type IV isotherm with two obvious hysteresis loops (**Fig. 5 A (b, c, d, e, f,** and **g)**), their N_2 adsorption capacities gradually decrease. Accordingly, their BET surface areas progressively decrease to 422.5 $m^2 \cdot g^{-1}$ for the ionogel PM-30 (**Table 1**). Their total pore volumes lower from 0.96 to 0.33 $cm^3 \cdot g^{-1}$. Moreover, their hysteresis loops near relative pressure P/P_0 = 0.30 gradually shift towards lower range, implying regularly reduced pore sizes (**Fig. 5 A (b, c, d, e, f,** and **g)**). Their corresponding pore size distributions are still narrow but regularly shift from 3.15 toward 2.14 nm (**Fig. 5 B (b, c, d, e, f,** and **g**) and **Table 1**). Taken the simulated dimensions (1.1×1.1×1.4 nm) of the IL into

Formatted: Font color: Auto
Formatted: Font color: Auto
Formatted: Font color: Auto
Formatted: Font color: Auto
Formatted: Font color: Auto
Formatted: Font color: Auto

consideration (**Fig. S4**), 0.05 g IL can ideally cover the maximum area of 132 m^2 in an ordered mono-molecule layer fashion. Thus, we believe that the IL $[P_{4444}][2\text{-Op}]$ prefers to dot the mesopores inside and produce as large interface as possible. The results well echo on the strong interfacial layering on the substrate investigated with submolecular resolution by high-energy X-ray reflectivity.[34] Most importantly, the progressively increased amounts of pores below 2.3 nm well coincide with the increasingly dotted IL in mesopores after we take the mean pore diameter (about 3.2 nm) of MCM-41 and the IL dimensions (1.1×1.1×1.4 nm) into account. It is noted that the hysteresis loop at low pressure of ionogel PM-45 disappears due to its mesopores completely filled or blocked with the IL $[P_{4444}][2\text{-Op}]$. Thus, an obvious decreasing in the amount of pores below 2.3 nm for PM-45 is reasonably found at a very low level (**Fig. 5 B (h)**). Additionally, no distinguishing change on the hysteresis loops above relative pressure P/P_0 = 0.40 is observed for ionogels PM-1, PM-3 and PM-5 (**Fig. 5 A (b, c,** and **d)**). The results imply that scarcely any IL $[P_{4444}][2\text{-Op}]$ is lined or dotted into macropores. However, the hysteresis loops above P/P_0 = 0.40 of PM-10, PM-15, PM-30, and PM-45 gradually lower as the amount of loaded IL above 10% (**Fig. 5 A (e, f, g**, and **h)**), implying that partial IL starts to coat the macropores. Correspondingly, their pore size distribution become broad and even shifts to micropore scale (**Fig. 5 B (e**, **f**, **g**, and **h)**). Their main pore diameters reduce from 2.61 nm to 1.92 nm. What's more, the pore volume of PM-45 is seriously lowered to 0.08 $cm^3 \cdot g^{-1}$ (**Table 1**). All the results confirm that the IL $[P_{4444}][2\text{-Op}]$ firstly lines in mesopores and subsequently macropores of the calcined supporter MCM-41.

3.6 Allosteric effects driven rapid CO_2 adsorption of the nanoconfined IL

Most surprisingly, low IL loading ionogels present significantly high CO_2 adsorption rates and capacities. Only less than 4 minutes is taken for the ionogel PM-5 to achieve saturation adsorption capacity of 1.21 $mmol \cdot (g\text{-Ionogel})^{-1}$ (**Fig. 6 A**), which is fairly shorter than several hours required for other reported ionogels and pristine bulk ILs.[24, 37-39] As far as we known, only a self-accelerating sorption of CO is recorded at low pressure of 80 kPa in a nanoporous crystal.[58] For the first time herein, the allosteric effects driven rapid CO_2 adsorption is observed on the nanoconfined IL $[P_{4444}][2\text{-Op}]$ at an ordinary pressure (**Fig. 6 A**). On the whole, it launches slowly and accelerates to run fast subsequently and goes down finally. The whole curve is tentatively divided into two *S*-shape stages by sharing the point of the middle lowest rate of 0.0071 $mmol \cdot (g\text{-Ionogel})^{-1} \cdot s^{-1}$ according to the evolution rhythm (Spot (**a**) in **Fig. 6 A**). Based on the calculation results of the Mulliken atomic charge, the oxygen atom of the loaded IL anion shows more

Formatted: Font color: Auto
Formatted: Font color: Auto
Formatted: Font color: Auto
Formatted: Font color: Auto
Formatted: Font color: Auto
Formatted: Font color: Auto

electronegative (–0.643) than the nitrogen one (–0.478) (**Table S1**). Further taken CO_2 preferring interaction to the electronegative oxygen into consideration,[28] the first small *S*-shape curve may contribute from the CO_2 uptake on the oxygen sites (Stage (**o–a**) stage in **Fig. 6 A**). The largest adsorption rate of 0.0118 mmol·(g-Ionogel)$^{-1}$·s^{-1} is observed in this stage. Its corresponding capacity is about 0.21 mmol·(g-Ionogel)$^{-1}$. Interestingly, the second *S*-shape curve in a large magnitude appears in the following process ((**a-b**) stage in **Fig. 6 A**). It is ascribed to the CO_2 interaction to the electronegative nitrogen atoms, which show poor accessibility in neutral pyridine for CO_2.[28, 59] The maximum adsorption rate of 0.0148 mmol·(g-Ionogel)$^{-1}$·s^{-1} is observed and the adsorption capacity is about 1.00 mmol·(g-Ionogel)$^{-1}$. Accordingly, about 82.0 % adsorption capacity is contributed from the electronegative nitrogen atoms despite of their trigger-required activity. Noticeably, the evolution rhythm of the stepwise adsorption rate in the ionogel PM-5 looks reminiscent of hemoglobin efficiently traps O_2 with the assistance of allosteric effects.

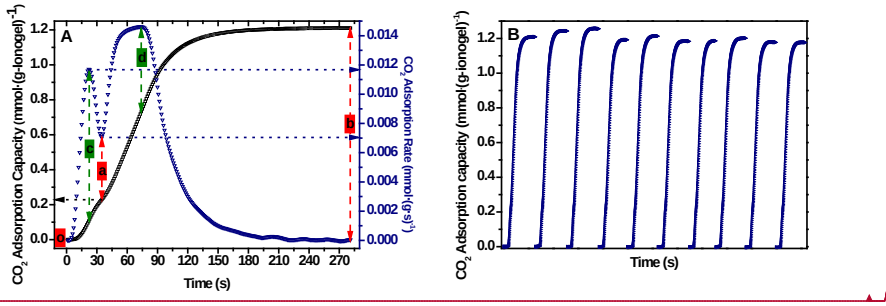

Fig. 6 (A) CO_2 adsorption capacity and rate of the ionogel PM-5 at 50 °C and constant pressure; (B) cycles of CO_2 adsorption capacity of the ionogel PM-5 at 50 °C

3.6 Loading-dependent capacity of CO_2 adsorption

Formatted: Font color: Auto
Formatted: Font color: Auto
Formatted: Font color: Auto
Formatted: Font color: Auto
Formatted: Font color: Auto
Formatted: Font color: Auto

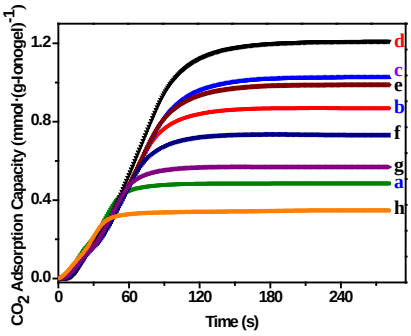

Fig. 7 CO_2 adsorption curves of samples at 50 °C (a) MCM-41, (b) PM-1, (c) PM-3, (d) PM-5, (e) PM-10, (f) PM-15, (g) PM-30, and (h) PM-45

All the ionogels with different loading amount exhibit steady adsorption capacity for CO_2 in less than 4 minutes at 50 °C (**Fig. 7**). After testing three batches of samples, we summarize their CO_2 adsorption capacity for further comparison (**Fig. 8**). In detail, the pure supporter MCM-41 exhibits a low CO_2 adsorption capacity of 0.49 mmol·g^{-1}, which can be ascribed to the oxygen-containing groups exposed on its surface (**Fig. 7(a)** and **Fig. 8**). After only loading 1% of the IL [P_{4444}][2-Op], the obtained ionogel PM-1 show an enhanced adsorption capacity as high as 0.87 mmol·(g-Ionogel)$^{-1}$ (38.49 mmol·(g-IL)$^{-1}$) in about 3 min, which is 78% higher than the pristine supporter (**Fig. 7(b)**). The results indicate that the highly dispersed IL in the supporter brings its functional groups into full play on the CO_2 adsorption. The adsorption capacity of ionogel PM-3 is more than two times that of the supporter (**Fig. 7(c)**). With increasingly loading the IL up to 5%, the highest CO_2 adsorption capacity of 1.21 mmol·(g-Ionogel)$^{-1}$ (14.89 mmol·(g-IL)$^{-1}$) among them is observed for the ionogel PM-5 in **Fig. 7(d)**. It is noteworthy to point out that our PM-5 possesses higher capacity 50 °C than that (0.905 mmol·(g-Ionogel)$^{-1}$) of MCM-41 impregnated with 50% [P_{66614}][2-Op] at 19 °C.[39] It can be induced that the IL is optimally dotted in the ionogel and its functional groups are efficiently accessible for gas molecules. The calculated Mulliken atomic electronegativity of both nitrogen and oxygen atoms of anion in our IL are higher than those in the reported IL [P_{66614}][2-Op] (**Table S1**).[28] What's more, their electronegativities are further enhanced after they are loaded onto the nanoporous silica surface. However, the adsorption capacity is lower than 3.706 mmol·(g-Ionogel)$^{-1}$ of the MCM-41 supported 60 % acrylamide-modified tetraethylenepentamine at 55 °C.[24, 38, 60] Thus, a higher adsorption capacity is much expectable basing on the results. More importantly,

Formatted: Font color: Auto
Formatted: Font color: Auto
Formatted: Font color: Auto
Formatted: Font color: Auto
Formatted: Font color: Auto
Formatted: Font color: Auto
Formatted: Font color: Auto
Formatted: Font color: Auto
Formatted: Font color: Auto
Formatted: Font color: Auto
Formatted: Font color: Auto
Formatted: Font color: Auto
Formatted: Font color: Auto

although its loading is very low, the adsorption performance of ionogel PM-5 at 50 °C fairly competitive with newly reported ionogels with high loading up to 10% – 50% (**Table S2**).[30, 37-40] With gradually further loading IL up to 30%, the adsorption capacities of PM-10, PM-15 and PM-30 inversely lower to 1.03, 0.90, and 0.57 mmol·(g-Ionogel)$^{-1}$ respectively (**Fig. 7(e**, **f**, and **g)** and **Fig. 8**), giving a hint of declining availability of functional groups. Similar changes are also observed in the Arg/PSS-PMMA sorbents.[42] The results coincide with loading-dependent status of the IL as oligomers or tiny clusters which show similar poor accessibility to guest molecules as the bulk IL. In case of the ionogel PM-45, its adsorption capacity is as poor as 0.35 mmol·(g-Ionogel)$^{-1}$, which is even lower than that of the supporter (**Fig. 7(h)** and **Fig. 8**). The result confirms that the loaded IL is so much enough to block or fulfill the pores and unavoidably impede the accessing of gas molecules. In the studies of mesoporous silica SBA-15 impregnated with IL of 1-ethyl-3-methylimidazolium tri[bis(trifluoromethylsulfonyl)imide]zincate and nanoporous PMMA supported IL [EMIM][Gly], analogous trends are also observed.[43, 47] Taken the small density (0.8507 g·cm^{-3}) of the IL into consideration, the calcined MCM-41 is dispersed in the bulk IL for the ionogel PM-45 rather than the IL is impregnated into the pores of MCM-41. Combining the poor thermal stability and low adsorption capacity of PM-30 and PM-45, the high IL loading does not always proportionally show high adsorption performance as expected. Obviously, fairly low cost is highly expected on the low IL loading ionogels with excellent cyclic stability and adsorption capacity.

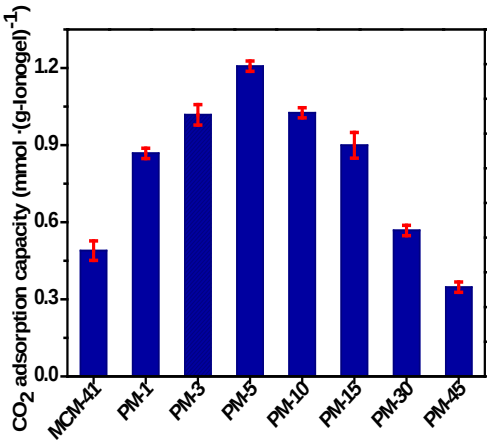

Fig. 8 CO_2 adsorption capacity at 50 °C from three batches of ionogels PM

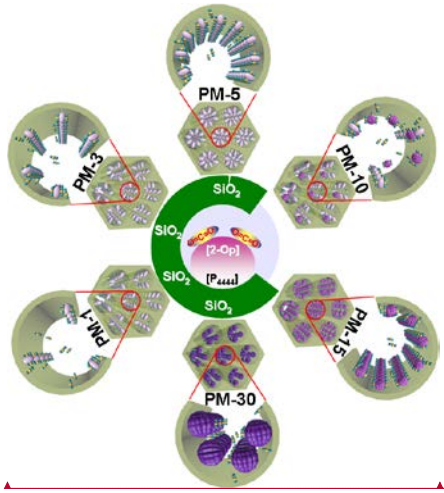

Fig. 9 Supposed mechanism of fabricating mesostructured ionogels by loading IL $[P_{4444}][2\text{-Op}]$ on the silica supporter MCM-41 and their CO_2 adsorption property.

3.8 Formation mechanism of the ionogels with different loading and their CO_2 adsorption

Based on the above observation, a formation mechanism of mesostructured ionogels and their adsorption performance is also proposed as following (**Fig. 9**): Pyridine-containing anion-functionalized IL $[P_{4444}][2\text{-Op}]$ with very low water content is firstly prepared and then infused into the calcined supporter MCM-41 with the given loading amount by using a moisture-controlled impregnation and evaporation approach. Using theoretical calculation, we find that the $[P_{4444}]^+$ prefers to line on the vicinity of the silica surface due to the its lower bounding energy of –41.8 kJ·mol^{-1} than that (–37.7 kJ·mol^{-1}) of $[2\text{-Op}]^-$ close to silica surface and that (–22.3 kJ·mol^{-1}) of the IL pair in staggered style (**Fig. S4**). The theoretical simulation on the surface electrostatic potential also indicates the preference of $[P_{4444}]^+$ of the IL close to the surface of silica MCM-41 (**Fig. S5**). The impregnated $[P_{4444}]^+$ is closely anchored even flatten to be more compatible with the rough mesopore walls due to the strong interfacial layering. At the same time, the $[2\text{-Op}]^-$ is able to well expose for the CO_2 attacking. The low loaded IL may present as sparse but completely exposed IL monomolecule islands in the ionogel, in which the ultra-large free space is enough for the occurrence of highly non-stoichiometric CO_2 adsorption (38.49 mmol·(g-IL)$^{-1}$). With the ascent of IL lining up to the threshold value of 5.0 %, more and more IL monomolecule islands become bumpy and their individual free spaces are partially squeezed. As a result, a non-stoichiometric but still high CO_2

Formatted: Font color: Auto

Formatted: Font color: Auto

adsorption of 14.89 mmol·(g-IL)$^{-1}$ is observed for the ionogel PM-5. As a whole, the CO_2 adsorption capacity increases in sequence with the increasing IL loading but below the threshold value of 5.0 %. An unprecedented enhancement on thermal stability up to 450 °C is perfectly recorded on the punctiformly lining IL confined in the nanoporous space of low loading ionogels. Especially, the allosteric effects driven adsorption make the stepwise CO_2 uptake process very fast due to the cooperative interaction between the multiple sites of electronegative oxygen and nitrogen atoms. The ionogel PM-5 shows the attractive CO_2 adsorption capacity up to 1.21 mmol·(g-Ionogel)$^{-1}$ and excellent cyclic stability after ten runs of sorption experiments. Many ILs for the separation of CO_2 from other gases such as N_2, are too expensive and inefficient to be economically viable. Here, the rapid adsorption of CO_2/N_2 mixtures can be achieved with a low cost on the ionogel PM-5 with sound stabilities. Due to the thronging IL up to 15%, one part of the IL prefers to discontinuously line as islands and another part states as oligomers or clusters which showing same properties as the bulk IL. The obtained high loading ionogels of PM-10 and PM-15 show not only two distinguishingly different onset decomposition temperatures but also the decreasing CO_2 adsorption capacities not as expected higher ones. Further high loading up to 30% or 45% makes the loading-dependent status of the immobilized IL gather as nanosized clusters, which fulfill the pores and show the same thermal stability to the bulk IL. It is not surprising that low surface area and pore volume only allow a poor CO_2 adsorption. In a summary, loading-dependent status of the IL companied with dramatically modified properties figure out that low content supported IL steadily show allosteric effects driven swiftly stepwise CO_2 sorption from a mixture with N_2 at a constant pressure.

3.10 Cyclic CO_2 adsorption stability of the nanoconfined IL

Excellent cyclic stability of an adsorbent is sometimes more important than high adsorption capacity for practical applications. Here, we take the ionogel PM-5 as a model to investigate the cyclic stability by performing 10 cycles of CO_2 adsorption. The specific CO_2 adsorption capacity of the ionogel PM-5 in each cycle is summarized in **Fig. S6**. After the ionogel PM-5 adsorbed CO_2 from the gas mixture with N_2, it is regenerated by heating up to 120 °C flowing N_2 for next cyclic experiment. One set of cyclic adsorption curves of ionogel PM-5 is selected as illustrated in **Fig. 6 B**. All the curves show similar adsorption process, implying the good cyclic stability. It can be seen that the adsorption capacity slightly differ in each cycle. The capacity only fluctuates from 1.21 to 1.17 mmol·(g-Ionogel)$^{-1}$ at the tenth cycle. More than 96% of the initial CO_2 uptake remained show an excellent cyclic stability and sorption reversibility.

The excellent cyclic stability can be attributed to the dramatically modified physicochemical property profiting from the low loading IL $[P_{4444}][2\text{-Op}]$ in the ionogel, such as strong interfacial layering, higher viscosity, lower dynamic and lower self-diffusion. All the properties cooperatively make the low loading IL perfectly anchored as monomolecule island on silica wall and possess excellent endurance to tough conditions such as high temperature, etc.

3.11 Influences of CO_2 partial pressure and temperature on the adsorption capacity

Accordingly, a typical coal-fired flue gas contains 76-77% N_2, 12.5-12.8% CO_2, 6.2% H_2O, 4.4% O_2, and trace amount of CO, NO_x, and SO_2 gases.[61] We further investigate the adsorption at different CO_2 partial pressure on the ionogel PM-5, which exhibits the highest uptake capacity with good cyclic stability at 50 ℃. In details, an adsorption capacity of 1.23 mmol·(g-Ionogel)$^{-1}$ is observed after exposing PM-5 at CO_2 partial pressure of 0.2510 (**Fig. 10 (a)**), which is close to that balancing at 0.1435 (**Fig. 10 (b)**). The adsorption capacities of PM-5 are 1.08 and 1.01 mmol·(g-Ionogel)$^{-1}$ at low partial pressures of 0.0988 and 0.0500, respectively (**Fig. 10 (c and d)**). Also, the lowest adsorption rate is calculated at the smallest partial pressure basing on the equilibrium time of 570 s. In general, both CO_2 adsorption capacity and rate decrease with decreasing partial pressure. Thus, the adsorption process is basically dominated by the diffusion limitation.

The operating temperature of the flue gas is generally be low 80 °C.[14, 61] In view of this point, the temperature dependence of final adsorption capacity is also studied on PM-5 at two different partial pressures in the temperature range of 30-70 ℃. It can be seen that the adsorption capacity decreases linearly with increasing temperature at the same partial pressure of 0.1435, with the highest (1.26 mmol·(g-Ionogel)$^{-1}$) at 30 ℃and the poorest one of 1.15 mmol·(g-Ionogel)$^{-1}$ at 70 ℃, respectively (**Fig. S7 (a)**). The change trend is reasonable and similar to the reported absorbent, which can be ascribed to the weakened interaction between the CO_2 to the PM-5 as the temperature rising.[43] The adsorption capacities of PM-5 are 1.13, 1.08 and 1.04 mmol·(g-Ionogel)$^{-1}$ at 30, 50 and 70 ℃recur the evolution rhythm at low partial pressures of 0.0988 (**Fig. S7 (b)**). All the results indicate that low temperature is helpful in obtaining high adsorption capacity.

Formatted: Font color: Auto
Formatted: Font color: Auto
Formatted: Font color: Auto
Formatted: Font color: Auto
Formatted: Font color: Auto
Formatted: Font color: Auto

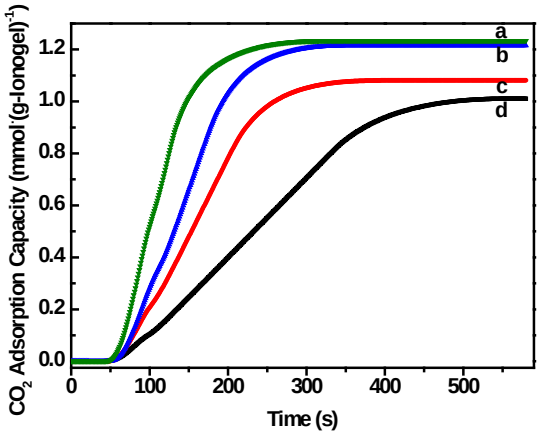

Fig. 10 CO_2 adsorption capacity of ionogel PM-5 at 50 °C recorded in gas mixture with different CO_2 partial pressure: (a) 0.2510, (b) 0.1435, (c) 0.0988, and (d) 0.0500.

4. Conclusions

A rare example of allosteric effect driven rapidly stepwise adsorption for CO_2 is demonstrated on the novel mesostructured ionogels $[P_{4444}][2\text{-Op}]$@MCM-41, which are fabricated by loading the pyridine-containing anion functionalized IL $[P_{4444}][2\text{-Op}]$ into the supporter MCM-41 through a moisture-controlled impregnation-evaporation method. Allosteric effect driven stepwise gas sorption on the electronegative oxygen and nitrogen atoms of the IL makes its 90 % of saturated adsorption capacity achieve in no more than 2 min. The ionogel PM-5 with the low IL $[P_{4444}][2\text{-Op}]$ lining of 5.0 % exhibits the highest CO_2 adsorption capacity up to 1.21 mmol·(g-Ionogel)$^{-1}$ among them and excellent cycling stability of more than 96% of the initial CO_2 uptake up to 10 cycles sorption. Also, an enhanced thermal stability up to 450 °C in N_2 is observed since the low loading IL supposedly lines as monomolecular islands in the silica nanospace. Reversely, the high loaded IL may aggregate into nanosized clusters and show the same thermal stability to the bulk IL. Although their surface area, pore volume and pore size regularly decrease with the IL loading up to 45%, the prepared ionogel PM-ws still show ordered hexagonal mesostructure. The low loading and cost, rapid adsorption, high capacity and excellent cyclic stability make the ionogel PM-5 a competitive candidate in CO_2 capture from the flue gas.

Formatted: Font color: Auto

Formatted: Font color: Auto

Acknowledgements

The authors acknowledge the financial supports from China Scholarship Council (No. 201506935028), Key Scientific and Technological Projects of Shanxi Province (No. MD2014-09), Natural Science Foundation of Shanxi Province (No. 2014011012-5), and Youth Foundation of Taiyuan University of Technology (No. 2015MS015).

References

1. S. Chu, *Science*, 2009, **325**, 1599-1599.
2. J. Wang, L. Huang, R. Yang, Z. Zhang, J. Wu, Y. Gao, Q. Wang, D. O'Hare and Z. Zhong, *Energy & Environmental Science*, 2014, **7**, 3478-3518.
3. Q. Wang, J. Luo, Z. Zhong and A. Borgna, *Energy & Environmental Science*, 2011, **4**, 42-55.
4. S. Li, Z. Wang, X. Yu, J. Wang and S. Wang, *Advanced Materials*, 2012, **24**, 3196-3200.
5. A. I. Cooper, *Nature*, 2015, **519**, 294-295.
6. C. Cai, H. Wang and J. Han, *Applied Surface Science*, 2011, **257**, 9802-9808.
7. G. Ferey, C. Serre, T. Devic, G. Maurin, H. Jobic, P. L. Llewellyn, G. De Weireld, A. Vimont, M. Daturi and J.-S. Chang, *Chemical Society Reviews*, 2011, **40**, 550-562.
8. N. MacDowell, N. Florin, A. Buchard, J. Hallett, A. Galindo, G. Jackson, C. S. Adjiman, C. K. Williams, N. Shah and P. Fennell, *Energy & Environmental Science*, 2010, **3**, 1645-1669.
9. G. T. Rochelle, *Science*, 2009, **325**, 1652-1654.
10. M. E. Boot-Handford, J. C. Abanades, E. J. Anthony, M. J. Blunt, S. Brandani, N. Mac Dowell, J. R. Fernandez, M.-C. Ferrari, R. Gross, J. P. Hallett, R. S. Haszeldine, P. Heptonstall, A. Lyngfelt, Z. Makuch, E. Mangano, R. T. J. Porter, M. Pourkashanian, G. T. Rochelle, N. Shah, J. G. Yao and P. S. Fennell, *Energy & Environmental Science*, 2014, **7**, 130-189.
11. J. Kou and L.-B. Sun, *Journal of Materials Chemistry A*, 2016, **4**, 17299-17307.

Formatted: Font color: Auto

12. J. Wang, I. Senkovska, M. Oschatz, M. R. Lohe, L. Borchardt, A. Heerwig, Q. Liu and S. Kaskel, *ACS Applied Materials & Interfaces*, 2013, **5**, 3160-3167.

13. L.-B. Sun, Y.-H. Kang, Y.-Q. Shi, Y. Jiang and X.-Q. Liu, *ACS Sustainable Chemistry & Engineering*, 2015, **3**, 3077-3085.

14. S. D. Kenarsari, D. Yang, G. Jiang, S. Zhang, J. Wang, A. G. Russell, Q. Wei and M. Fan, *RSC Advances*, 2013, **3**, 22739-22773.

15. Y. Zeng, R. Zou and Y. Zhao, *Advanced Materials*, 2016, **28**, 2855-2873.

16. P.-Q. Liao, X.-W. Chen, S.-Y. Liu, X.-Y. Li, Y.-T. Xu, M. Tang, Z. Rui, H. Ji, J.-P. Zhang and X.-M. Chen, *Chemical Science*, 2016, **7**, 6528-6533.

17. Y. Yue, J. A. Rabone, H. Liu, S. M. Mahurin, M.-R. Li, H. Wang, Z. Lu, B. Chen, J. Wang, Y. Fang and S. Dai, *The Journal of Physical Chemistry C*, 2015, **119**, 9442-9449.

18. H. Wang, B. Li, H. Wu, T.-L. Hu, Z. Yao, W. Zhou, S. Xiang and B. Chen, *Journal of the American Chemical Society*, 2015, **137**, 9963-9970.

19. Z. Chang, D.-H. Yang, J. Xu, T.-L. Hu and X.-H. Bu, *Advanced Materials*, 2015, **27**, 5432-5441.

20. C. Serre, S. Bourrelly, A. Vimont, N. A. Ramsahye, G. Maurin, P. L. Llewellyn, M. Daturi, Y. Filinchuk, O. Leynaud, P. Barnes and G. Férey, *Advanced Materials*, 2007, **19**, 2246-2251.

21. X. Zhang, X. Zhang, H. Dong, Z. Zhao, S. Zhang and Y. Huang, *Energy & Environmental Science*, 2012, **5**, 6668-6681.

22. M. Ramdin, T. W. de Loos and T. J. H. Vlugt, *Industrial & Engineering Chemistry Research*, 2012, **51**, 8149-8177.

23. J. Zhang, C. Jia, H. Dong, J. Wang, X. Zhang and S. Zhang, *Industrial & Engineering Chemistry Research*, 2013, **52**, 5835-5841.

24. C. Wang, X. Luo, X. Zhu, G. Cui, D.-e. Jiang, D. Deng, H. Li and S. Dai, *RSC Advances*, 2013, **3**, 15518-15527.

25. S. Supasitmongkol and P. Styring, *Energy & Environmental Science*, 2010, **3**, 1961-1972.

26. I. H. Harvey Arellano, J. H.; Pendleton, P., *RSC Adv.*, 2015, **5**, 65074-65083.

27. F. Z. Wang, Z. Q.; Yang, J.; Wang, L. P.; Lin, Y.; Wei, Y., *Fuel*, 2013, **107**, 394-399.

28. X. Luo, Y. Guo, F. Ding, H. Zhao, G. Cui, H. Li and C. Wang, *Angewandte Chemie International Edition*, 2014, **53**, 7053-7057.

29. L. C. Tome and I. M. Marrucho, *Chemical Society Reviews*, 2016, **45**, 2785-2824.

30. Y. Yu, J. Mai, L. Huang, L. Wang and X. Li, *RSC Advances*, 2014, **4**, 12756-12762.

31. A. I. Horowitz and M. J. Panzer, *Angewandte Chemie International Edition*, 2014, **53**, 9780-9783.

32. M.-A. Néouze, J. L. Bideau, P. Gaveau, S. Bellayer and A. Vioux, *Chemistry of Materials*, 2006, **18**, 3931-3936.

33. L. J. Lozano, C. Godínez, A. P. de los Ríos, F. J. Hernández-Fernández, S. Sánchez-Segado and F. J. Alguacil, *Journal of Membrane Science*, 2011, **376**, 1-14.

34. M. Mezger, H. Schroder, H. Reichert, S. Schramm, J. S. Okasinski, S. Schoder, V. Honkimaiki, M. Deutsch, B. M. Ocko, J. Ralston, M. Rohwerder, M. Stratmann and H. Dosch, *Science*, 2008, 424.

35. B. Coasne, L. Viau and A. Vioux, *The Journal of Physical Chemistry Letters*, 2011, **2**, 1150-1154.

36. S. Perkin, T. Albrecht and J. Klein, *Physical Chemistry Chemical Physics*, 2010, **12**, 1243-1247.

37. Y. Zhou, J. Liu, M. Xiao, Y. Meng and L. Sun, *ACS Applied Materials & Interfaces*, 2016, **8**, 5547-5555.

38. J. Zhang, S. Zhang, K. Dong, Y. Zhang, Y. Shen and X. Lv, *Chemistry – A European Journal*, 2006, **12**, 4021-4026.

39. J. Cheng, Y. Li, L. Hu, J. Zhou and K. Cen, *Energy & Fuels*, 2016, **30**, 3251-3256.

40. M. M. Wan, H. Y. Zhu, Y. Y. Li, J. Ma, S. Liu and J. H. Zhu, *ACS Applied Materials & Interfaces*, 2014, **6**, 12947-12955.

41. A. S. Aquino, F. L. Bernard, J. V. Borges, L. Mafra, F. D. Vecchia, M. O. Vieira, R. Ligabue, M. Seferin, V. V. Chaban, E. J. Cabrita and S. Einloft, *RSC Advances*, 2015, **5**, 64220-64227.

42. B. Jiang, X. Wang, M. L. Gray, Y. Duan, D. Luebke and B. Li, *Applied Energy*, 2013, **109**, 112-118.

43. X. Wang, N. G. Akhmedov, Y. Duan, D. Luebke and B. Li, *Journal of Materials Chemistry A*, 2013, **1**, 2978-2982.

44. S. Lee, S.-Y. Moon, H. Kim, J.-S. Bae, E. Jeon, H.-Y. Ahn and J.-W. Park, *RSC Advances*, 2014, **4**, 1543-1550.

45. I. H. Arellano, S. H. Madani, J. Huang and P. Pendleton, *Chemical Engineering Journal*, 2016, **283**, 692-702.

46. I. H. Arellano, J. Huang and P. Pendleton, *RSC Advances*, 2015, **5**, 65074-65083.

47. I. H. Arellano, J. Huang and P. Pendleton, *Chemical Engineering Journal*, 2015, **281**, 119-125.

48. J. W. Ren, L. B.; Li, B. G., *Industrial & Engineering Chemistry Research*, 2012, **51**, 7901-7909.

49. M. B. Yue, Y. Chun, Y. Cao, X. Dong and J. H. Zhu, *Advanced Functional Materials*, 2006, **16**, 1717-1722.

50. M. P. Singh, R. K. Singh and S. Chandra, *Progress in Materials Science*, 2014, **64**, 73-120.

51. S. Chen, G. Wu, M. Sha and S. Huang, *Journal of the American Chemical Society*, 2007, **129**, 2416-2417.

52. S. Chen, K. Kobayashi, Y. Miyata, N. Imazu, T. Saito, R. Kitaura and H. Shinohara, *Journal of the American Chemical Society*, 2009, **131**, 14850-14856.

53. A. K. Tripathi, Y. L. Verma and R. K. Singh, *Journal of Materials Chemistry A*, 2015, **3**, 23809-23820.

54. C. T. Kresge, M. E. Leonowicz, W. J. Roth, J. C. Vartuli and J. S. Beck, *Nature*, 1992, **359**, 710-712.

55. Y. Wan and Zhao, *Chemical Reviews*, 2007, **107**, 2821-2860.

56. D. Zhao, J. Feng, Q. Huo, N. Melosh, G. H. Fredrickson, B. F. Chmelka and G. D. Stucky, *Science*, 1998, **279**, 548-552.

57. C. Xue, B. Tu and D. Zhao, *Advanced Functional Materials*, 2008, **18**, 3914-3921.

58. H. Sato, W. Kosaka, R. Matsuda, A. Hori, Y. Hijikata, R. V. Belosludov, S. Sakaki, M. Takata and S. Kitagawa, *Science*, 2014, **343**, 167-170.

59. P. Singh, J. P. M. Niederer and G. F. Versteeg, *Chemical Engineering Research and Design*, 2009, **87**, 135-144.

60. X. Zhang, X. Zheng, S. Zhang, B. Zhao and W. Wu, *Industrial & Engineering Chemistry Research*, 2012, **51**, 15163-15169.

61. N. Du, H. B. Park, M. M. Dal-Cin and M. D. Guiver, *Energy & Environmental Science*, 2012, **5**, 7306-7322.

Formatted: Font color: Auto